Ann. Geophysicae 18, 223–234 (2000) © EGS – Springer-Verlag 2000

Annales Geophysicae

4D tropospheric tomography using GPS slant wet delays

A. Flores, G. Ruffini, A. Rius

Institut d'Estudis Espacials de Catalunya (IEEC), CSIC Research Unit Edif. Nexus-204, Gran Capità 2-4, 08034 Barcelona, Spain
E-mail: flores@ieec.fcr.es

Received: 1 February 1999 / Revised: 16 September 1999 / Accepted: 21 September 1995

Abstract. Tomographic techniques are successfully applied to obtain 4D images of the tropospheric refractivity in a local dense network of global positioning system (GPS) receivers. We show here how GPS data are processed to obtain the tropospheric slant wet delays and discuss the validity of the processing. These slant wet delays are the observables in the tomographic processing. We then discuss the inverse problem in 4D tropospheric tomography making extensive use of simulations to test the system and define the resolution and the impact of noise. Finally, we use data from the Kilauea network in Hawaii for February 1, 1997, and a local $4 \times 4 \times 40$ voxel grid on a region of 400 km^2 and 15 km in height to produce the corresponding 4D wet refractivity fields, which are then validated using forecast analysis from the European Center for Medium Range Weather Forecast (ECMWF). We conclude that tomographic techniques can be used to monitor the troposphere in time and space.

Key words: Radio science (remote sensing; instruments and techniques)

1 Introduction

Tomographic techniques aim to obtain a solution field from integrated measurements along different ray paths. They have been successfully applied, for instance, in seismic and oceanographic studies, using earthquake and accoustic sensing; two dimensional images of the ionosphere using radio signals from polar orbiting satellites and dedicated receivers have also been described (see e.g. Raymund *et al.*, 1994). The global positioning system (GPS) globally and continuously transmits radio signals, which are affected by the presence of the atmosphere and hence carry information on its state. Thus, GPS signals can be used as data for 4D atmospheric tomography. While global ionospheric four dimensional maps have been described earlier (see e.g. Ruffini *et al.*, 1998b; Howe *et al.*, 1998), the application of tomography to the troposphere has required a refinement in the processing techniques of GPS data in order to obtain the tropospheric slant delays, due to their non-dispersive nature and smaller magnitude. The higher spatial and temporal variability of the troposphere demands small dense networks to be used for tomographic purposes. The tomographic 4D distribution of the troposphere obtained using GPS signals can be used for the calibration of other remote sensing techniques (e.g. SAR) and in numerical weather prediction models as additional data. We present the first results of tropospheric tomography using a dense ground network of GPS receivers, providing evidence that this technique can yield horizontal and vertical structure of the wet refractivity.

The effect of the atmosphere on GPS signals appears as an extra delay in the measurement of travel time from the transmitters to the receiver. The ionospheric electron content produces a dispersive delay and can hence be corrected by using two different frequencies and linearly combining them. The neutral atmosphere, however, induces an excess delay independent of frequency. This delay (ΔL) can be related to the neutral refractivity (N) by:

$$\Delta L = \int_{s.l.} 10^{-6} N \, \mathrm{d}l \ , \tag{1}$$

$$N = 77.6\frac{P}{T} + 64.8\frac{P_w}{T} + 3.776 \cdot 10^5 \frac{P_w}{T^2} + 1.4W \tag{2}$$

$$= N_h + N_w + 1.4W \ , \tag{3}$$

where $10^{-6}N$ can be expressed in mm/km, *s.l.* stands for the slant path through the atmosphere, P is the total atmospheric pressure in mbar, P_w is the water vapour

Correspondence to: A. Flores

pressure in mbar, T is the atmospheric temperature in K (Smith and Weintraub, 1953; Thayer, 1974), and W is the liquid water vapour in the atmosphere. The latter term is generally neglected (Kursinski, 1997). N_h and N_w are the hydrostatic and wet refractivities. This slant delay is usually modelled as a zenith component (zenith total delay, ZTD) multiplied by a mapping function that acounts for the dependence on the elevation, plus a horizontal gradient to consider the azimuthal variability of the atmosphere. The time evolution of these parameters is modelled as a random walk stochastic process.

The total atmospheric delay can be split into two components: the *hydrostatic delay*, due to the dry gases in the troposphere and the nondipole component of water vapour, and the *wet delay*, due to the dipole component of water vapour (Thayer, 1974). The refractivity is also divided into hydrostatic and wet components, as shown in Eq. 3. The spatio-temporal structure of wet refractivity cannot be correctly modelled from surface measurements.

Here we consider slant wet delays (SWD) (Ware *et al.*, 1997; Rocken *et al.*, 1993) as the observables of the tomography to obtain 4D fields of the wet refractivity. We first describe the approach taken to estimate the SWDs using the Jet Propulsion Laboratory's software GIPSY-OASIS II (GOA II) (Webb and Zumberge, 1997) and ECMWF analysis. Then we briefly describe the inverse problem and the solution process. Since for tropospheric tomography a small-scale dense network is needed, we take the geometry of the permanent Kilauea network in Hawaii (mainly devoted to volcanic studies, Owen, 1997) as the reference for simulation-based analysis of the resolution of the system and the impact of noise. Finally, we take GPS data measured in this network for one particular day (1 February, 1997) and apply the described techniques to yield wet refractivity 4D fields which are compared against ECMWF analysis.

2 The tropospheric slant wet delays

The GPS transmits at two frequencies $f_1 = 1.57542$ GHz and $f_2 = 1.2276$ GHz. The corresponding phase delay measurements L_1 and L_2 can be linearly combined to remove the effect of the ionosphere (Spilker, 1978). The resulting observable L_C is modelled in GOA II as the contribution of the geometrical delay, receiver and transmitter clock errors, tropospheric effects, antenna phase pattern, an integer number of cycles and noise:

$$\begin{aligned} L_C = {} & \text{geometric delay} - \text{station clock error} \\ & + \text{satellite clock error} \\ & + \text{antenna phase pattern delay} \\ & + \text{tropospheric delay} + \text{noise} \end{aligned} \tag{4}$$

We use a precise point positioning (Zumberge *et al.*, 1997) approach in which precise satellite clock corrections and GPS satellites orbits are provided by JPL, as well as Earth orientation parameters that are used to transform coordinates from an Earth-fixed reference frame to the inertial one in which orbits are given. In the estimation process, the position of the station is considered as a constant bias from an apriori position obtained with a long term solution, the station clock bias is modelled as a white noise stochastic process and the antenna phase pattern is an input to the system. Tropospheric delays (L_t) are modelled as the contribution of a zenith component plus horizontal gradients, both estimated as a random walk processes, and they can hence be written as (Davis *et al.*, 1993):

$$\begin{aligned} L_t = {} & m_h(e)\left[L_z^h + \cot e\left(G_N^h \cos\phi + G_E^h \sin\phi\right)\right] \\ & + m_w(e)\left[L_z^w + \cot e\left(G_N^w \cos\phi + G_E^w \sin\phi\right)\right] \end{aligned} \tag{5}$$

where L_z^h and L_z^w are the hydrostatic and wet zenith delays, e and ϕ are the satellite elevation and azimuth as seen from the station, respectively; G_N^h, G_N^w, G_E^h and G_E^w are the north and east components of the hydrostatic and wet delay gradients; m_h and m_w are the hydrostatic and wet mapping functions (we use Niell mapping functions, Niell, 1996). The zenith hydrostatic delay (ZHD) can be removed using surface pressure measurements (see Elgered *et al.*, 1991 for details). The removal of the ZHD reduces the scale height of the problem, since typically the hydrostatic component has a scale height of about 8 km while the wet component has roughly a 2 km scale height. In order to obtain the slant wet delays, the hydrostatic gradients must also be removed from the solution using external measurements or analysis since they cannot be discriminated from the wet gradients in the GPS data processing. The gradient parameters G_N and G_E in Eq. 5 have units of path delay and are site-dependent parameters defined as (Davis *et al.*, 1993)

$$\mathbf{G} = 10^{-6} \int_0^\infty \mathrm{d}z\, z\mathbf{g}(z) \ , \tag{6}$$

where $\mathbf{g}(z) = \nabla_\rho N(\rho, z)|_{\rho=0}$ is the horizontal gradient of the refractivity, ρ is the horizontal displacement vector, and z is the height above the surface. However, as shown in Elósegui *et al.* (1999) and in Ruffini *et al.* (1999) a gradient of the zenith component can be as well computed as

$$\mathbf{Z} = 10^{-6} \int_0^\infty \mathrm{d}z\, \mathbf{g}(z) \ , \tag{7}$$

and has units of path delay per unit distance. The relationship between $\mathbf{G}$ and $\mathbf{Z}$ for the hydrostatic case can be obtained by assuming an exponential law in the hydrostatic refractivity, leading to $\mathbf{G} = H\mathbf{Z}$, where H is the scale height. For the particular case that we are using, we used the analysis of ECMWF to obtain the surface pressures, estimate the ZHD at each station and then compute the $\mathbf{Z}$ to finally obtain the value of $\mathbf{G}$ (another approach for removing the hydrostatic gradient is described in Bar-Sever and Kroger, 1998, where they are considered to be constant over periods of 12 h and hence they can be removed by averaging the gradient solution over that period and demeaning it).

The removal of hydrostatic gradients is a key step in the processing, because it has a direct impact on the interpretation of the 4D fields retrieved with tomography. Let us now consider that zenith hydrostatic delays are removed using surface pressure measurements with a 1 mbar accuracy and that hydrostatic gradients are not removed. In such a case, one would be dealing with *pseudo-wet delays* as observables and one would be retrieving the *pseudo-wet refractivity* field, which to first order can be written as

$$\hat{N}(z,\rho,t) = N_w(z,t) + \mathbf{g}_w(z,t)\cdot\rho + \Delta N_{oh}(z,t) + \mathbf{g}_h(z,t)\cdot\rho \ , \quad (8)$$

where $\Delta N_{oh}(z,t)$ stands for the refractivity error due to the 1 mbar accuracy of the surface pressure measurements, $\mathbf{g}_h(z,t)$ is the horizontal hydrostatic refractivity gradient and $\mathbf{g}_w(z,t)$ is the horizontal wet refractivity gradient. Therefore, if one considers this to be the real wet refractivity, the total error is:

$$\Delta N(z,\rho,t) = \Delta N_{oh}(z,t) + \mathbf{g}_h(z,t)\cdot\rho \ . \quad (9)$$

The value of $\Delta N_{oh}(z,t)$ introduces a random error in the field of about 0.1% in the surface value of N. The unremoved hydrostatic gradient, $\mathbf{g}_h(z,t)$, on the other hand, appears in the solution as a systematic tilt in the direction of the hydrostatic gradient. The relevance of this tilt is a function of the relative magnitudes of the wet and dry gradients. In the case of the Hawaii network, surface horizontal gradients of the wet and hydrostatic refractivity fields are on the order of $0.5\,\mathrm{N\,km^{-1}}$ and $0.005\,\mathrm{N\,km^{-1}}$ respectively (the latter computed as described; note that the 0.5° grid of the ECMWF analysis does not allow for large gradients in a local scale; in a dedicated campaign, however, there should be surface pressure measurements). Therefore, there are two orders of magnitude between both kinds of gradients and we can assume the smaller to be negligible with respect to the other. However, we stress the importance of removing the hydrostatic delay gradients using ancillary data such as on-site measurements or weather forecast analyses; otherwise one should be aware that the results are *pseudo-wet refractivity* fields which may significantly differ from *wet refractivity* under conditions of strong surface pressure gradients (which could no longer be considered negligible).

Once all hydrostatic parameters are removed, we model the tropospheric wet delay as

$$L_{wt} = m_w(e)L_z^w + m_w(e)\cot e\left(G_N^w\cos\phi + G_E^w\sin\phi\right) \ , \quad (10)$$

and the time dependences of L_z^w and $\mathbf{G} = (G_N, G_E)$ are modelled as a random walk stochastic process, with a drift rate of $0.25\,\mathrm{cm}/\sqrt{s}$ for the zenith component and $0.03\ \mathrm{cm}/\sqrt{s}$ for the gradients (Bar-Sever and Kroger, 1998). We then form the slant wet delays (SWD) by mapping back the zenith wet delay and the gradients to each ray direction and adding the post-fit residues to each measurement. This recreates the individual slant delay measurement which may include unmodelled effects such as the 3D distribution of the water vapour, particularly at low elevations, as well as unmodelled noise. In fact, the increased scatter of the post-fit residuals at low elevations reveals a possible deficiency in the mapping functions. Not including the residuals would introduce errors into the tomographic solution due to the angle dependencies of the wet delays described by the mapping functions. Moreover, the decomposition of the refractivity into a zenith component plus a horizontal gradient is a first-order approximation, which may fail to describe some refractivity structures. The addition of the post-fit residuals, however, may also mean the addition of multipath noise, clock errors, coordinate errors, and phase noise to the observables. Let us now consider these errors and how they map into the observables. The phase noise is accounted for in the data processing using GOA II by assigning a 2 mm sigma value to the observations. This yields a formal variance of the zenith wet delay estimation of about 0.5 cm ($\sigma \approx 1$ cm in the slant direction). This uncertainty is considered in the covariance matrix of the observables in tomography. Coordinate errors (≈2 mm, and considering that the vertical coordinate is not highly correlated with the atmospheric delay, since we use a long term solution for the position), clock errors and multipath at each station included in the GOA II post-fit residues are uncorrelated from one station to another since we use a precise point positioning strategy; the combination of all rays in the tomographic solution will also remove the uncorrelated noise from the solution. In contrast, mapping function mismodelling contributes a systematic uncorrelated error to the observables. We can therefore conclude that the addition of the post-fit residuals is needed and that the noise that they add is usually below the formal uncertainty of the observables and also uncorrelated with the wet troposphere structure. We will see in Subsect. 3.2 how this noise in the observables is considered in the numerical implementation of the inverse problem. Results with real data from the network in Hawaii confirm this discussion, as we will see.

3 Tomographic approach and resolution

3.1 The inverse problem

In the inverse problem one considers the observations (**y**) as the basis to obtain the values of some parameters (**x**) that are related to them through a model (**A**). This can be written using matrix notation as $\mathbf{y} = \mathbf{A}\mathbf{x}$. Tomography is a particular case of the inverse problem in which measurements are the integration of the model parameters along ray paths. Generally, the discrete inverse theory formulation (Menke, 1989) is used. To this end, we rewrite the solution field (wet refractivity in our case, N_w) as a linear combination of a set of basis functions (Φ),

$$N_w(\mathbf{r},t) = \sum_j x_j(t)\Phi_j(\mathbf{r}) + \epsilon(\mathbf{r},t) \ , \quad (11)$$

where $\mathbf{r}$ is the position vector of the point considered, x_j are the time-dependent coefficients of the linear combination and ϵ is the quantisation error. In our tomographic approach, we use a finite set of three dimensional voxels which are given a value of one in a defined volume and zero elsewhere. This set defines a local grid that spans over the region below 15 km that is scanned by the rays with a 7° elevation cutoff, where we will consider our solution fields to be confined. Then, our observations (y_i) are modelled by

$$y_i(t) = \int_{s.l.} N_w(\mathbf{r},t)\mathrm{d}l = \sum_j x_j(t) \int_{s.l.} \Phi_j(\mathbf{r})\mathrm{d}l + \zeta(\mathbf{r},t) \ , \quad (12)$$

where y_i is in millimetres, $\mathrm{d}l$ is in kilometres (notice that we removed the 10^{-6} factor), *s.l.* stands for the slant path distance inside the grid, and $\zeta(\mathbf{r},t)$ is the integral of the quantisation error. If we ignore this latter term, each of the terms can be placed as a row in a linear system of the form

$$\mathbf{y} = \mathbf{A}\mathbf{x} \quad (13)$$

where $a_{ij} = \int_{s.l._i} \Phi_j(\mathbf{r})\mathrm{d}l$, and $s.l._i$ is the slant path of ray i (in the present analyses we have considered no curvature effect on the rays, a valid option for ground receivers but invalid if we dealt with the Low Earth Orbiting receiver sounding data). The goal is now to invert this system and solve for $\mathbf{x}$. In general, we will have many more observations than unknowns (model parameters). We obtain the least-squares solution by minimising the functional

$$\chi^2 = (\mathbf{y} - \mathbf{A}\mathbf{x})^T C_y^{-1} (\mathbf{y} - \mathbf{A}\mathbf{x}) \quad (14)$$

assuming diagonal covariance matrix for the observations and with equal uncertainties. When assuming a Gaussian distribution for the error in the observations, the least-squares solution is the maximum likelihood solution. This expression can be reduced to

$$x = \left[\mathbf{A}^T C_y^{-1} \mathbf{A}\right]^{-1} C_y^{-1} A^T \mathbf{y} \ . \quad (15)$$

Although performing the inversion of this matrix may not be possible, a generalised inverse form can be found using singular value decomposition (Menke, 1989), which is a powerful tool for analysing the resolution of the system, as we will describe in the next subsection.

The system, however, may be underdetermined even though the number of equations exceeds the number of unknowns. This is so because, for example, a voxel in the grid may not be crossed and thus be undetermined. In previous work (see Ruffini *et al.*, 1998) we discussed the use of a correlation functional to confine the spatial spectrum of the solution to the low portion of the frequency space; that is, not allowing sharp changes in the spatial distribution of the solution. The same concept can be expressed by adding new equations that impose that the refractivity in a voxel be a weighted average of its neighbours (*smoothing constraints*, see Rius *et al.*, 1997):

$$0 = w_1 x_1 + \cdots + w_{j-1} x_{j-1} - x_j + w_{j+1} x_{j+1} + \cdots \quad (16)$$

and include them in the linear system as additional observation equations with some overall weighting (λ). It can be easily shown that the solution is now

$$x = \left[\mathbf{A}^T C_y^{-1} \mathbf{A} + \lambda \mathbf{B}^T \mathbf{B}\right]^{-1} C_y^{-1} A^T \mathbf{y} \ , \quad (17)$$

where $\mathbf{B}$ is the set of equations like Eq. 16. In fact, we will use three types of constraints: horizontal smoothing, vertical smoothing and boundary conditions (the latter only applied to the highest layer), with three different weights, tuned using the procedure described later.

Finally, in order to account for the time variation of the parameters, we implement a Kalman filtering with backward smoothing as described in Herring *et al.* (1990) and considering the refractivity values' time evolution as a random walk stochastic process with a drift rate of $\delta = 5\,\mathrm{mm}/(\mathrm{km}\sqrt{(h)})$.

3.2 Resolution using singular value decomposition

In order to obtain the inverse matrix shown in Eq. 17 we use the singular value decomposition (SVD), as is described, e.g. in Menke (1989), Hajj *et al.* (1994), and Ruffini *et al.* (1998), and the numerical implementation described in Press *et al.* (1997). We give here only a short review of the SVD.

The SVD technique computes the eigenvalues of the system and identifies the null space of the solution, characterised by zero eigenvalues. An $\mathrm{N} \times \mathrm{M}$ matrix $\mathbf{A}$ is decomposed as:

$$\mathbf{A} = \mathbf{U}\Lambda\mathbf{V}^T \ , \quad (18)$$

where $\mathbf{U}$ is a orthonormal $\mathrm{N} \times \mathrm{N}$ matrix of eigenvectors that span the data space, Λ is an $\mathrm{N} \times \mathrm{M}$ diagonal eigenvalues matrix (arranged in decreasing order) and $\mathbf{V}$ is an $\mathrm{M} \times \mathrm{M}$ matrix of eigenvectors that span the model parameter space. The generalised inverse (see Menke, 1989) is formed using the non-zero eigenvalues:

$$\mathbf{A}^{-g} = \mathbf{V}\Lambda^{-1}\mathbf{U}^T \ , \quad (19)$$

where in Λ^{-1} the corresponding values of zero eigenvalues are set to zero and not to infinity. The zero eigenvalues correspond to model parameters (voxels) not fixed by the data. If we want a solution to be well defined, then there should not be any zero eigenvalues. Furthermore, small eigenvalues due to computational round-off errors or a very low sensitivity of the data to a particular combination of model parameters produce a large variance in the solution, since the covariance matrix of the solution is

$$\mathbf{C}_x = \sigma_d^2 \mathbf{V}\Lambda^{-2}\mathbf{V}^T \quad (20)$$

$$\sigma_d^2 = \frac{(y - Ax)^T C_y^{-1} (y - Ax)}{N_{obs} - N_{unk}} \ , \quad (21)$$

where N_{obs} is the number of observations and N_{unk} is the number of unknowns. As discussed in Hajj *et al.* (1994) and Rius *et al.* (1997), this can be translated into an amplification of the input noise into the solution by a factor given by the smallest non-zero eigenvalue. We can then consider that $\sigma_x \approx \sigma_y / v$ where v is the smallest non-zero eigenvalue, σ_x^2 is the variance of the solution and σ_y^2 is that of the data. This sets a cutoff value for the values in Λ. Introducing smoothing constraints actually increases the value of all the eigenvalues, due to the inherent enlargement of the effective size of those voxels where there are not sufficient observations. We therefore must set the weight of the constraints (λ in Eq. 17) to the minimum value that makes all the eigenvalues greater than the cutoff level. As stated, we use three sets of constraints because, depending on the geometry of the network and the variability of the refractivity, horizontal smoothing may not be enough: as an example, one can imagine a network of ground receivers, all at the same horizontal plane, and consider a rectangular geometry with a refractivity field that does not have any horizontal variation, but some vertical structure. Then, the interchange of two different layers would lead to the same integrated delay measurements and therefore, we could not distinguish between both solutions. Setting the upper boundary layer to be zero (something reasonable for the water vapour at 15 km altitude) and imposing vertical smoothing (equally valid as the horizontal smoothing) helps in such situations. The different weights are tuned following the eigenvalue cutoff criteria defined.

Let us now compute this cutoff value for the case of wet tropospheric tomography. The water vapour content is characterised by the mixing ratio r expressed in g/kg. Following Kursinski (1997) and Houghton (1979), at mid-latitudes the relative error in current estimations of r is $\Delta r / r = 10\%$, and a typical value on ground of $r \approx 5$ g/kg, and thus, an typical uncertainty of $\Delta r \approx 0.5$ g/kg. Using standard ground values for the rest of parameters, and the expressions (N_w in mm/km, r in g/kg),

$$P_w = \frac{Pr}{0.622} \quad , \tag{22}$$

$$N_w = \frac{373}{0.622} r \frac{P}{T^2} \quad , \tag{23}$$

this translates into an uncertainty of $\Delta N_w = \sigma_x \approx 3.5$ mm/km. Taking $\sigma_y = 10$ mm, as we discussed in a previous section, the cutoff value for the eigenvalues of $\mathbf{A}$ is $v > 2.8$ km, which implies a cutoff value of $w = v^2 > 8.1\,\mathrm{km}^2$ for the inversion of $\mathbf{A}^T C_y^T \mathbf{A} + \lambda \mathbf{B}^T \mathbf{B}$. We will hence tune λ until all eigenvalues are greater than $8.1\,\mathrm{km}^2$.

Now, what does the 2.8 km cutoff value mean? It is, in fact, the shortest effective length that a ray has to cross in the grid to provide information above the noise level. This, however, is an effective length, since we combine rays in each Kalman filtering batch and they go across the same voxels, the noise is averaged out and thus, the minimum length is then $2.8/\sqrt{N}$ where N is the mean number of rays hitting the same voxel during a Kalman batch. Through simulations, we have found that this number for a 30 min batch is roughly 50 for all batches, and thus, this sets a minimum realistic thickness of the layers in the grid of 350 m.

4 Simulations using the Kilauea network

We have developed a software package, LOcal Tropospheric TOmographic Software (LOTTOS), that in-

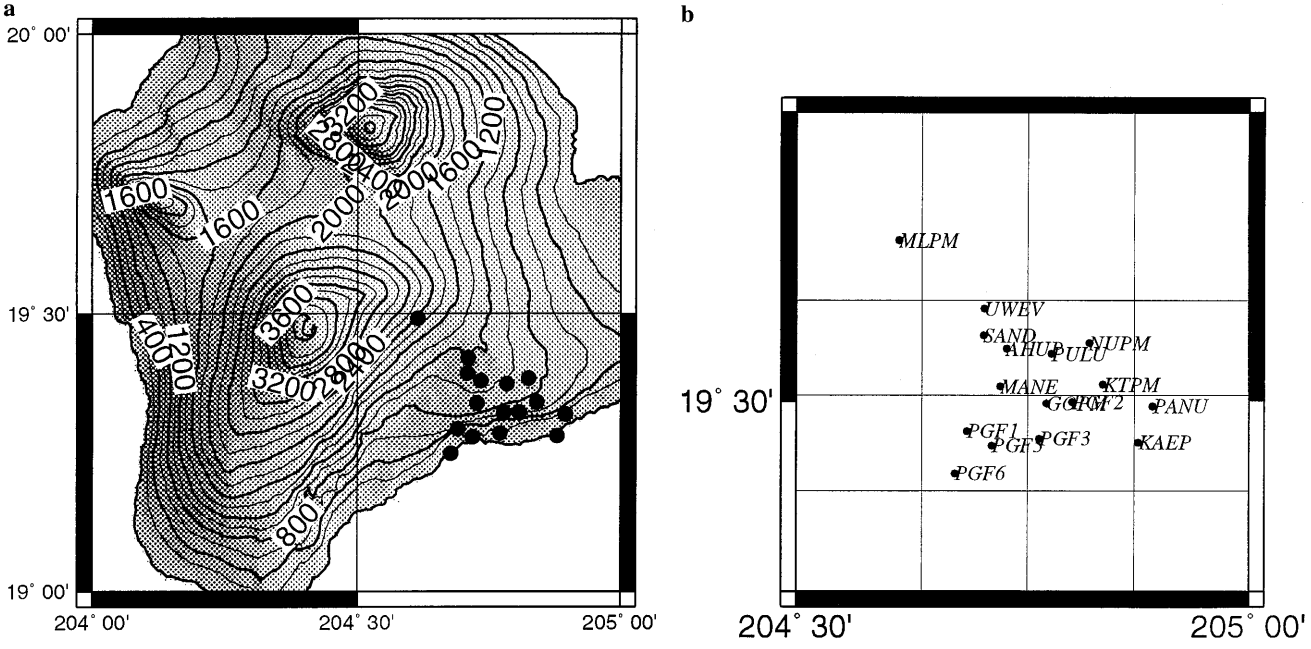

Fig. 1. Map with the location of the stations of the Kilauea permanent network in Hawaii in February 1997 (*left*) and representation of the grid (*right*)

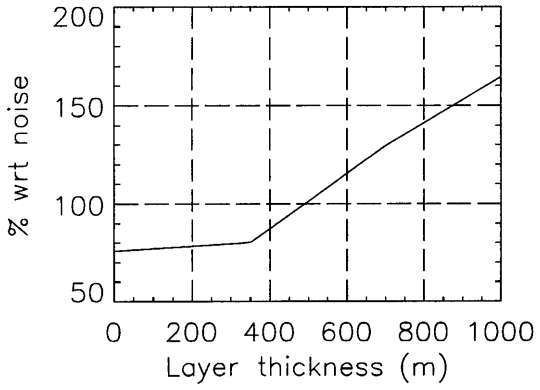

Fig. 2. Discretisation error. Rms value of the residuals, normalised to the nominal noise level in the observables, as a function of layer thickness

cludes the tomographic processing as well as interfaces with the GOA II file formats and simulation capabilities. The LOTTOS software has been used to analyse simulated fields and the impact of noise, and to process the real data. In this section we present the results using simulated fields.

The Kilauea network in Hawaii is a dense local network, normally used to track ground movements due to volcanic activity (Owen, 1997). We had available a set of data used to study these movements (January 30 eruption) and for this tropospheric study we have selected a date (February 1, 1997) when those had vanished. There are 16 stations distributed over an area of 400 km^2 (see Fig. 1) and located at different heights that range from sea level up to about 2000 m; the elevation cutoff angle was 7°. The height distribution is an essential factor to obtain good vertical resolution. For the simulations, we have used the locations of the stations and the satellite orbits for that day.

In order to determine the impact of the discretisation error, we first define a regular grid of 7×7 voxels in the horizontal and 82 layers of 175 m thick up to 15 km height above the sea level to generate the delays. In the horizontal a small gradient has been applied and in the vertical the profile given by a radiosonde launched somewhere else has been used. Additive Gaussian noise has also been included. The gradient is small enough so that when a more coarse grid in the horizontal is used (4×4) the discretisation error is below the additive noise; in this way we can analyse the impact of layer thickness separately from the horizontal dimension. The delays thus generated have been used as observables in a tomographic solution using a grid of 4×4 voxels in the

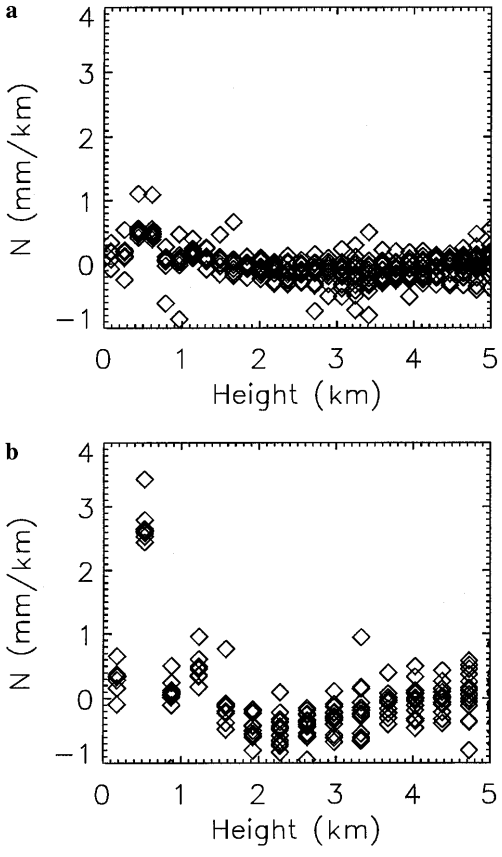

Fig. 3. Spike analysis: response to a 3.5 mm/km spike in the profile at all horizontal cells at 350 m height with width 175 m (*top*) and 350 m (*bottom*). The noise was $\sigma = 10$ mm for both. A *symbol* is plotted for each horizontal cell at a given height

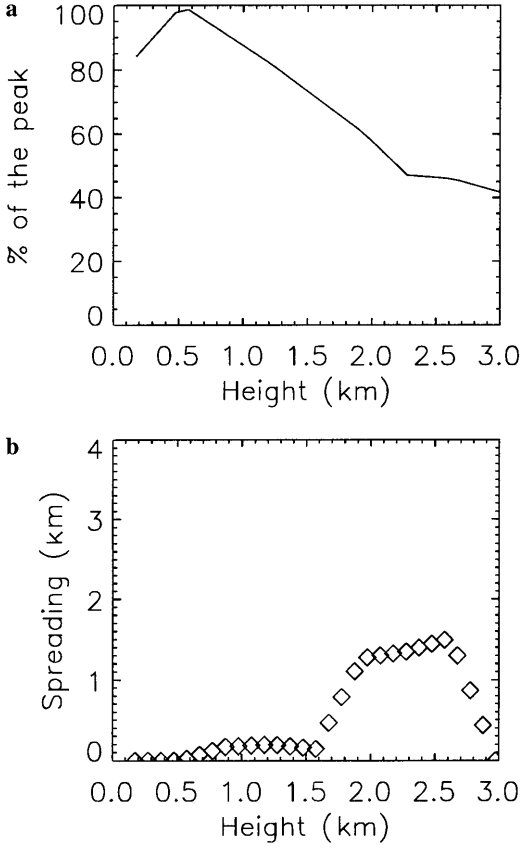

Fig. 4. Spike analysis: response to a 3.5 mm/km spike located at different heights. In the *upper plot* we show the value of the peak obtained in the solution relative to 3.5 mm/km. In the *lower plot*, the evolution of width of the peak down to 60% of the maximum value. The spreading in the lower heights is limited by the good reconstruction capabilities for data at ≈600 m

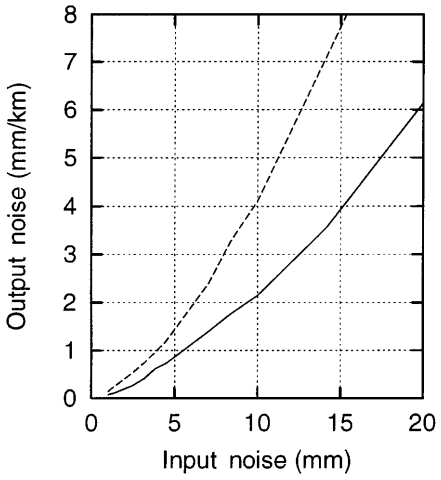

Fig. 5. Impact of noise in the solution. *Solid line* is for a cutoff value of $v = 2.8$ km and the *dashed line* for $v = 1.41$ km

horizontal and successively thicker layers. For each run, the rms value of the residues has been computed. In Fig. 2 we show the evolution of this value normalised to the input random noise (in %) as a function of the layer thickness. It is shown that using 350 m thick layers implies a discretisation noise below the input random noise.

The vertical resolution has also been tested using a spike analysis. We have previously discussed how measurement noise limits the vertical resolution to 350 m layers. In order to verify this, we have considered a 3.5 mm/km spike of 175 m thick first, and then of 350 m thick. As we show in Fig. 3, the former is almost lost in the reconstructed field while the latter can be recognized. We have carried out further simulations with the spike of 350 m thickness placed at different heights and results are presented in Fig. 4. The parameters computed are the spread of the spike (width of the peak to 60% of its maximum value) and the relative value of the peak in the solution with respect to the original 3.5 mm/km. It can be seen that resolution is gradually lost as we move to higher altitudes: the peak spreads and it becomes barely noticeable. It should be noted that at lower heights the peak is reconstructed at 85% of its height and there is no spreading; this shows that at about 600 m high the reconstruction is almost perfect.

This analysis has been carried out using the Kilauea network, which has a unique vertical distribution of

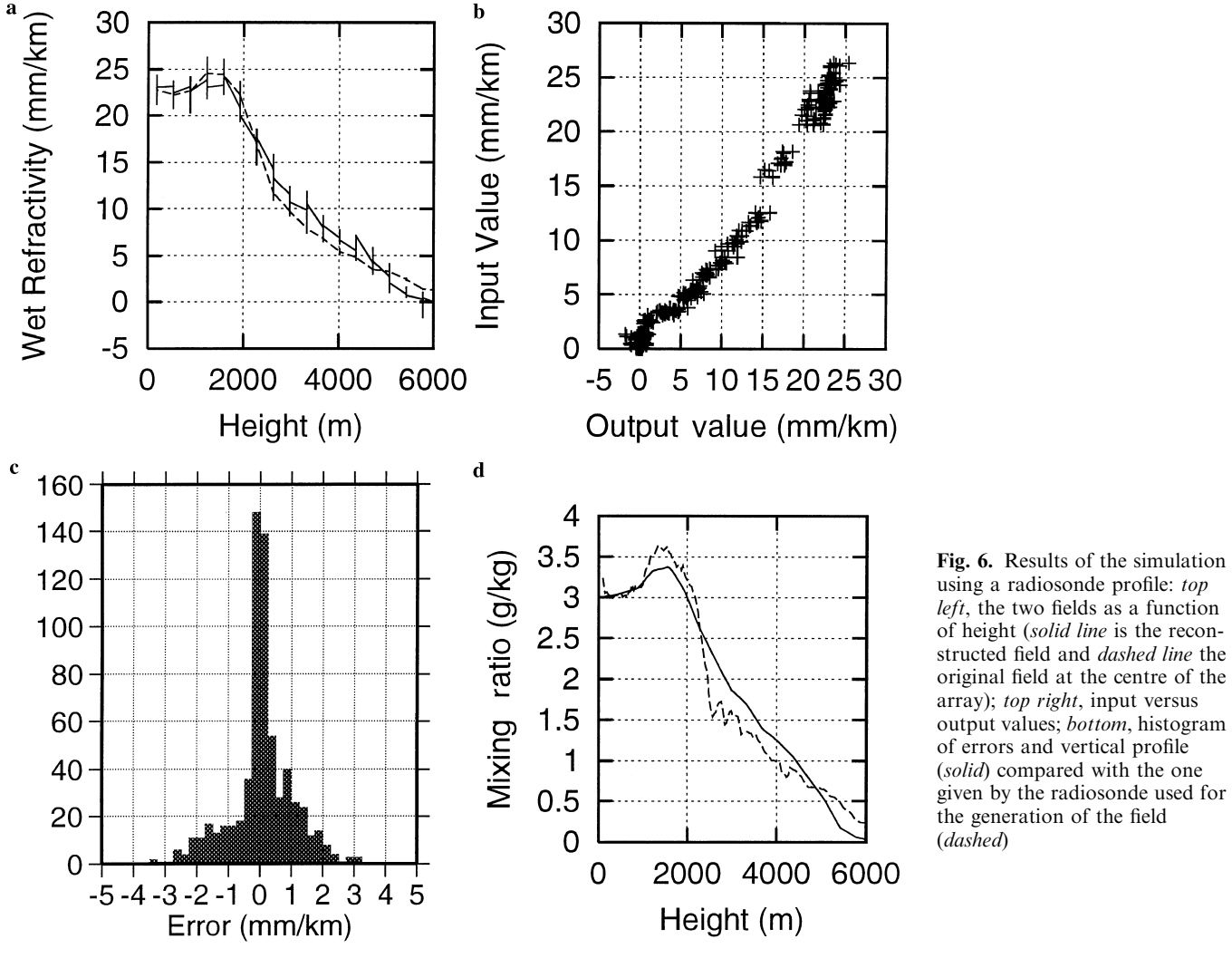

Fig. 6. Results of the simulation using a radiosonde profile: *top left*, the two fields as a function of height (*solid line* is the reconstructed field and *dashed line* the original field at the centre of the array); *top right*, input versus output values; *bottom*, histogram of errors and vertical profile (*solid*) compared with the one given by the radiosonde used for the generation of the field (*dashed*)

stations. We leave for future work the analysis of the impact of different geometries for a completely flat GPS receiver network.

The impact of noise has been tested. We have fixed the grid to $4 \times 4 \times 40$ voxels and generated the data with the same grid to remove the discretisation error. Because the system is linear, we can consider here only a Gaussian white noise sequence as the input data. The noise power ranged from $1\,\text{mm}^2$ to $10^4\,\text{mm}^2$. For each series, the rms error in the refractivity field has been computed. In Fig. 5 we show the relationship between both parameters, with two different cutoff values. The solid line is for a $v = 2.8\,\text{km}$ cutoff value and the dashed line corresponds to $v = 1.4\,\text{km}$. In the 10 mm input noise range, the linear relationship is clearly seen and as well as the corresponding factor 2 between the output noise for both cases.

Finally, we present simulations considering two different atmospheric conditions. In all the simulations we have included Gaussian white noise ($\sigma_n = 10$ mm) added to each ray.

In the first simulation we have synthesised a refractivity field based on the vertical profile given by the radiosonde measurement mentioned already, and superimposed a horizontal linear gradient.

We have defined a $4 \times 4 \times 40$ voxel grid over the area. The amount of data spanned 30 min, to simulate the Kalman filter batches. The weights of the three constraints are tuned so that no eigenvalue is below the cutoff threshold of $8.1\,\text{km}^2$. The evolution of the eigenvalues is shown in Fig. 7. We show the eigenvalues without any constraints, and then successively add horizontal and (strong) vertical smoothing constraints, horizontal smoothing and boundary condition and finally vertical and horizontal smoothing and a boundary condition. It can be seen that all three are needed in order to provide enough constraint on all the unknown parameters. The third plot shows that applying very strong smoothing constraints also raises the eigenvalues, but in such a case the solution field would have a larger level of residues; therefore the tuning of the weights has to also consider the level of the residues. With this implementation the tomographic inversion has provided the results shown in Fig. 6. The reconstruction follows the original field well within the 3.5 mm/km error upper bound. The histogram of errors shows a high spike around the zero value corresponding to the higher layers of the field. Finally, the comparison of the mixing ratio profile with the one given by the radiosonde reveals that tomography can provide the stated vertical resolution (below 6 km), though it is not as fine as a radiosonde. As a second example, we have used the vertical profile given by GPS/MET occultation data processed for an occultation at 49.2°S, 303.26°E on June 23, 1995, at 04:07 UT (the profile was provided by E.R. Kursinksi, and appears in Kursinski, 1997; details on the occultation mission and data processing can be found in Rocken *et al.*, 1997; Kursinski 1997; Ware *et al.*, 1996). These data were selected because of the irregular vertical structure. Regarding the horizontal variability, we applied a non-linear distribution. Results are presented

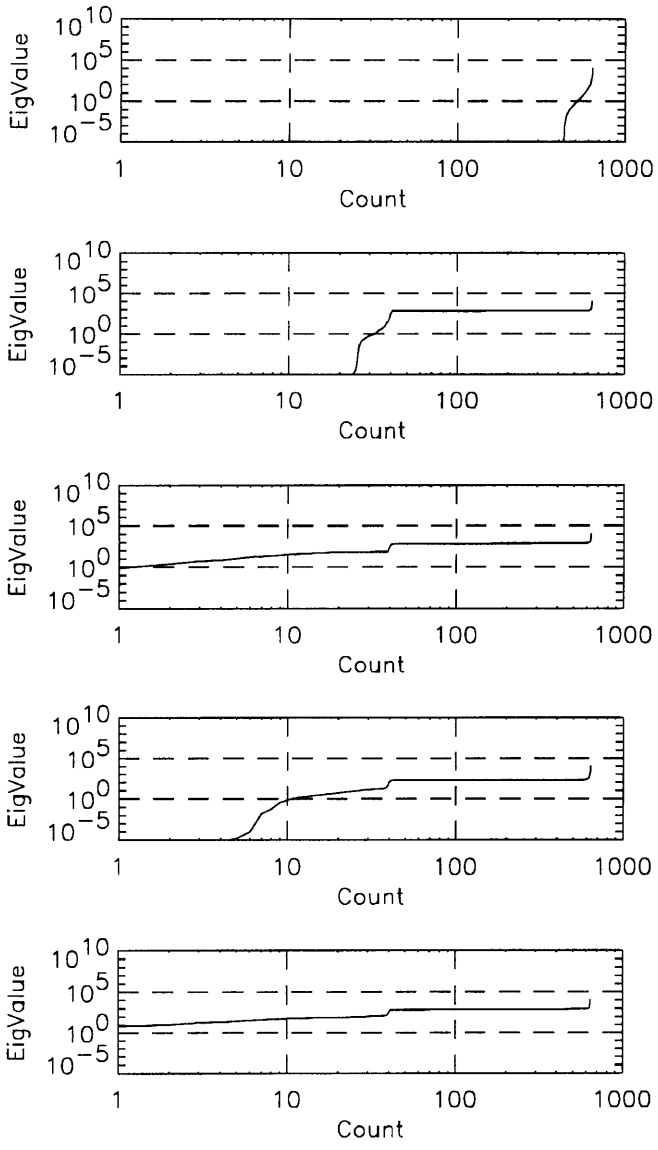

Fig. 7. Evolution of eigenvalues without any constraints (*top*), with horizontal constraints, horizontal and (strong) vertical, horizontal and boundary and with all constraints (*bottom*). The case with strong vertical smoothing shows that when the constraints have too much weight the eigenvalue condition can also be met, although the solution would not have a good fit with data

in Fig. 8 and they show similar features as in the previous case. However, in this case, the vertical structure has a sharp increase in humidity at low altitudes and then a hump at around 4 km. As shown in Fig. 4, using 30 min of data vertical resolution is gradually lost as the spike is placed at higher altitudes; this undesirable effect has been minimised by using longer batches of data (60 min). This reveals a tradeoff between spatial and temporal resolution.

5 Results using data from the Kilauea network

We have processed data from 16 stations in the permanent Kilauea network for February 1, 1997. We

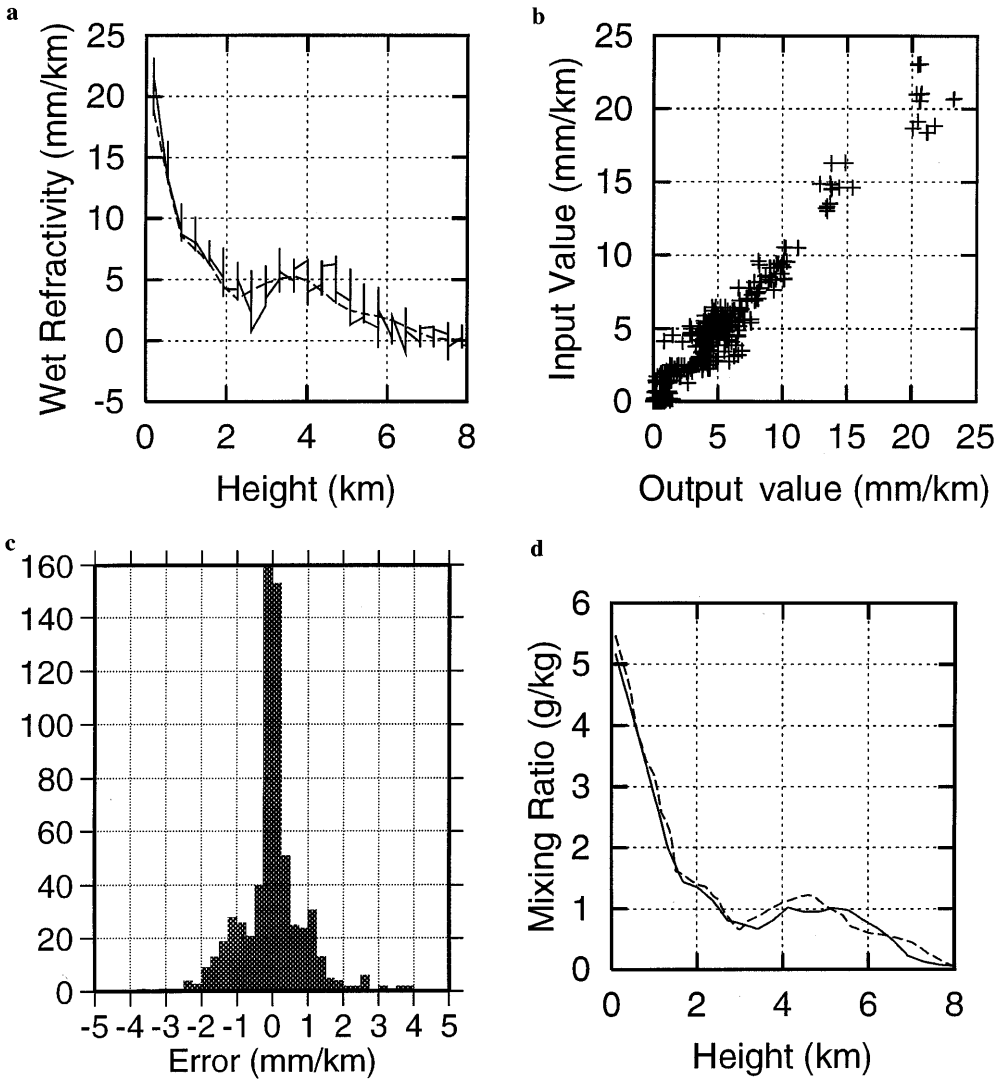

Fig. 8. Results of the simulation using a GPS/MET occultation: *top left*, the two fields as a function of height (*solid line* is the reconstructed field and *dashed line* the original field at the centre of the array); *top right*, input versus output values; *bottom*, histogram of errors and vertical profile (*solid*) compared with the one given by the radiosonde used for the generation of the field (*dashed*)

have used a grid of 4×4 voxels ($6'$ in latitude and $7'$ in longitude), 40 layers of 350 m thick and 30-min batches for the Kalman filter. The GPS data have been processed using GOA II. In Fig. 9 we present the histogram of the residuals ($\sigma = 7.6$ mm). The time series of zenith wet delay, gradients and residuals have been combined to yield the SWD. In order to calibrate the weights of the constraints we have followed the same procedure as in the simulations. The residues of the tomographic fields are shown in a histogram in Fig. 10 ($\sigma = 6.1$ mm) and in Fig. 11 their dependence with elevation, together with the GOA processing residuals. These results show that the tomographic solution represents a better fit in the determination of the 4D distribution of wet refractivity; it is worth mentioning that the elevation dependence of the post-fit residues in both cases is very small, which indicates an atmosphere well modelled by the mapping functions in this experiment; nevertheless, they do not have the same dependence and this is due to the difference between the Niell mapping function used in GOA II and the mapping function implicit in our implementation of tomography based on voxels and without considering the ray bending (we have kept the system simple to verify the

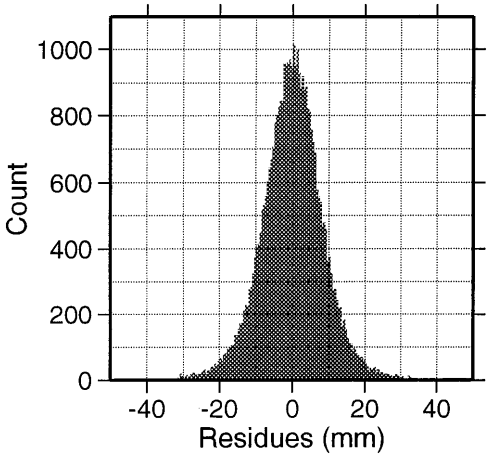

Fig. 9. Histogram of the residues of the GOA II processing ($\sigma = 7.6$ mm)

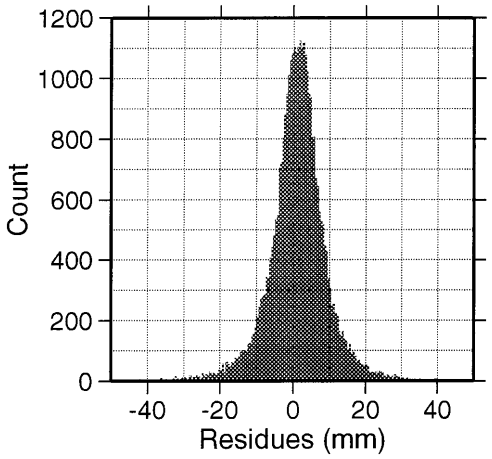

Fig. 10. Histogram of the residues of the tomographic processing ($\sigma = 6.1$ mm)

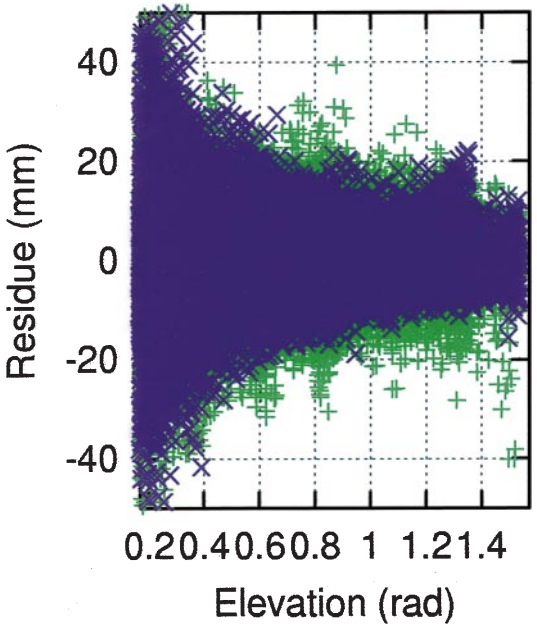

Fig. 11. Dependency of the residues of the GOA II processing (*green*) and tomography (*blue*) with respect to elevation. The tomographic solution shows a smaller scatter of residuals though roughly the same elevation dependence. This is due to good agreement of the mapping function with the structure of the atmosphere for this particular case

capabilities of tomography). In order to prove that the obtained fields are compatible with the GOA II parameters, we have reconstructed the SWD from the tomographic fields and then calculated the time series of the horizontal delay gradients and ZWD for each station. These have been compared to those obtained with GOA II from the original data. In Fig. 12 we show the time series of the ZWD and the two components of the delay gradient for a particular station (PGF3) and in Table 1 we show the correlation values over time for each station. This, however, just demonstrates the consistency between solution and data over the time span. The vertical refractivity field is shown in Fig. 13 for latitude 19°16′ and for times between 14:00–

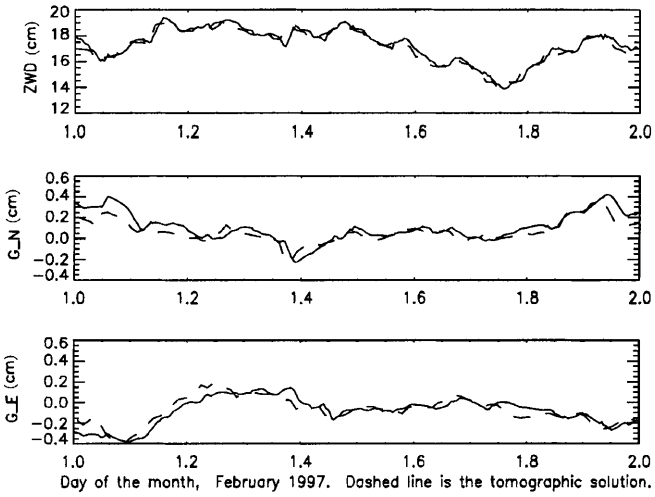

Fig. 12. Comparison of the time series of the GOA II solution and the tomographic solution (*dashed*). The good matching ensures that the tomographic field fits well with the time of the input data

Table 1. 24-h correlation factors between the parameters retrieved using the GOA II processing on the actual data and on data generated using the tomographic fields. The ZWD and the total horizontal gradients in both components, north and east, are shown for each station

Station	ZWD	North	East
AHUP	0.98	0.80	0.83
GOPM	0.96	0.79	0.64
KAEP	0.98	0.78	0.71
KTPM	0.97	0.57	0.72
MANE	0.98	0.90	0.70
MLPM	0.99	0.55	0.88
NUPM	0.97	0.62	0.53
PANU	0.99	0.53	0.43
PGF1	0.98	0.83	0.83
PGF2	0.97	0.74	0.78
PGF3	0.97	0.86	0.86
PGF5	0.97	0.85	0.84
PGF6	0.97	0.88	0.89
PULU	0.98	0.56	0.41
SAND	0.99	0.61	0.82
UWEV	0.99	0.69	0.82

14:30 UT. In order to verify this structure, we have computed the values of $N_w(\mathbf{r}, t)$ profiles from the ECMWF analysis and compared them with our tomographic profiles taking a mean value of all the voxels in the horizontal plane to meet the ECMWF map resolution of 0.5 degrees. Results are presented in Fig. 14 for the three different time stamps (06 h, 12 h, and 18 h) for which we have the ECMWF maps, showing good agreement. It can also be seen that ECMWF forecasts predict a smoother time variation than tomography shows, which is expected given the unpredictable behaviour of the water vapour content in the troposphere. The differences between ECMWF forecasts and tomography cannot be taken as a direct reflection of the quality of the tomographic solution, given the great difference in resolution between the two. No comparison with radiosonde data was done due to the unavailability

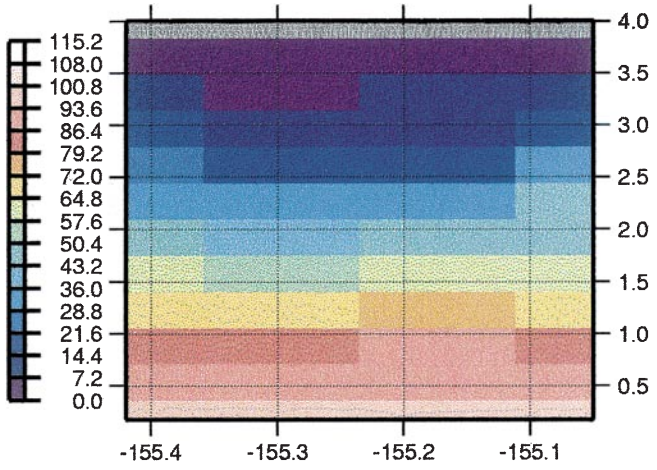

Fig. 13. Cross section of the tomographic solution for latitude 19°16′, and 14:00–14:30 UT

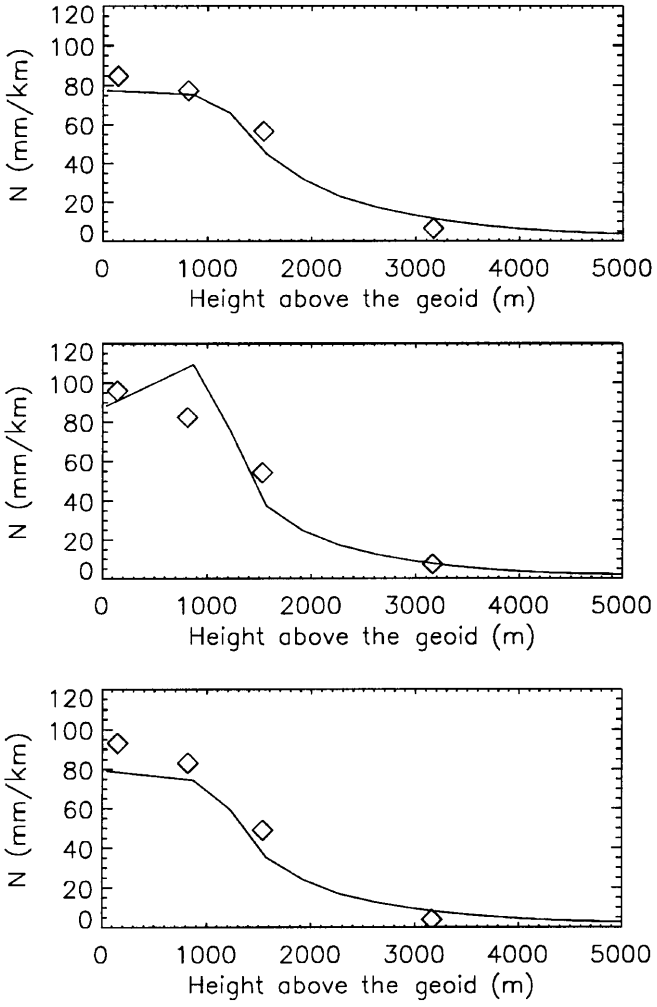

Fig. 14. Comparison of the tomographic wet refractivity profile (*solid line*) with the ECMWF analysis (*diamonds*) for the same area at times 06 h, 12 h and 18 h. ECMWF analyses have a poorer time and space resolution

of such data in the area considered for the day processed.

6 Conclusions

Tropospheric tomography has been confirmed as a practical approach to the description of the spatio-temporal structure of water vapour in the atmosphere. We have presented the principles of the technique, an analysis of the impact of random and discretisation noise, and extensive work using simulations based on real vertical profiles and spike analysis, demonstrating that the system can resolve perturbations of 3.5 mm/km in the vertical profile refractivity at heights less than 4 km. We have developed the software LOTTOS for retrieving the tomographic solution and applied it to data from the permanent Kilauea network in Hawaii for 1 February, 1997. The tomographic solution provides a small improvement in variance over simple ZWD and gradient parametrisation ($\sigma = 6.1$ mm versus $\sigma = 7.6$ mm); in addition, the profiles obtained agree with ECMWF analysis and the solution has a much greater spatio-temporal resolution. This study has been carried out based on this network and there is certainly more work to be done regarding flat networks and with a smaller number of GPS receivers. In flat networks, the system could be aided using external measurements such as radiosondes or NWP models to enhance the vertical resolution.

Acknowledgements. We thank the USGS Hawaii Volcano Observatory, Stanford University and the University of Hawaii, and JPL for providing the data. We thank Yoaz Bar-Sever (JPL) for useful conversations, Rob Kursinski (JPL) for providing the GPS/MET occultation profile, Chris Rocken (UCAR) for many useful comments, Beatriz Navascués (Instituto Nacional de Meteorología) for providing the ECMWF data and the anonymous referees for their comments and suggestions. This work was supported by Spanish Climate CICYT grant CLI95-1781, EC grant WAVEFRONT PL-952007 and the Comissionat per a Universitats i Recerca de la Generalitat de Catalunya.

Topical Editor J. P. Duvel thanks J. S. Haase and another referee for their help in evaluating this paper.

References

Bar-Sever, Y. E., and P. M. Kroger, Estimating horizontal gradients of tropospheric path delay with a single GPS receiver, *J. Geophys. Res.*, **103,** 5019–5035, 1998.

Davis, J. L., G. Elgered, A. E. Niell, and C. E. Kuehn, Ground-based measurement of gradients in the "wet" radio refractivity of air, *Radio Sci.*, **28,** 1003–1018, 1993.

Elgered, G., J. L. Davis, T. A. Herring, and I. I. Shapiro, Geodesy by radio interferometry: water vapour radiometry for estimation of the wet delay, *J. Geophys. Res.*, **96,** 6541–6555, 1991.

Elósegui, P., J. L. Davis, L. P. Gradinarsky, G. Elgered, J. M. Johansson, D. A. Tahmoush, and A. Rius, Sensing atmospheric structure using small-scale space geodetic networks, *Geophys. Res. Lett.*, **26,** 2445–2448, 1999.

Hajj, G. A., R. Ibañez-Meier, E. R. Kursinski, and L. J. Romans, Imaging the ionosphere with the global positioning system, *Intl. J. Imag. Syst. Tech.*, **5,** 174–184, 1994.

Herring, T. A., J. L. Davis, G. Elgered, and I. I. Shapiro, Geodesy by radio interferomtery: the application of Kalman filtering to the analysis of very long baseline interferometry data, *J. Geophys. Res.*, **95,** 12 561–12 581, 1990.

Houghton, J. T., *The physics of atmospheres*, Cambridge University Press, Cambridge, UK, 1979.

Howe, B., K. Runciman, and J. A. Secan, Tomography of the ionosphere: Four-dimensional simulations, *Radio Sci.*, **33,** 109–128, 1998.

Kursinski, R. E., The GPS radio occultation concept: theoretical performance and initial results, PhD Dissertation Thesis, California Institute of Technology, Pasadena CA 1997, USA.

Menke, W., *Geophysical data analysis: discrete inverse theory*, Revised Edn, International Geophysics Series, **45,** Academic Press, New York, 1989.

Niell, A. E., Global mapping functions for the atmospheric delay at radio wavelengths, *J. Geophys. Res.*, **101,** 3227–3246, 1996.

Owen, S., http://pangea.stanford.edu/owen/kilauea.html, 1997.

Press, W. H., S. A. Teukolsky, W. T. Vetterling, and B. P. Flannery, *Numerical recipes in Fortran. The art of scientific computing*. Cambridge University Press, 4th edn, 1997.

Raymund, T. D., S. J. Franke, and K. C. Yeh, Ionospheric tomography: its limitations and reconstruction methods, *J. Atmos. Terr. Phys.*, **56,** 637–657, 1994.

Rius, A., G. Ruffini, and L. Cucurull, Improving the vertical resolution of ionospheric tomography with GPS occultations, *Geophys. Res. Lett.*, **24,** 2291–2295, 1997.

Rocken, C., R. H. Ware, T. Van Hove, F. Solheim, C. Alber, J. Johnson, M. Bevis, and S. Businger, Sensing atmospheric water vapour with the global positioning system, *Geophys. Res. Lett.*, **20,** 2631–2634, 1993.

Rocken, C., R. Anthes, M. Exner, D. Hunt, S. Sokolovsky, R. Ware, M. Gurbunov, W. Schreiner, D. Feng, B. Herman, Y.-H. Kuo, and X. Zou, Analysis and validation of GPS/MET data in the neutral atmosphere, *J. Geophys. Res.*, **102,** 29 849–29 866, 1997.

Ruffini, G., A. Flores, and A. Rius, GPS tomography of the ionospheric electron content with a correlation functional, *IEEE Trans. Geos. Remote Sensing*, **36,** 143–153, 1998a.

Ruffini, G., E. Cardellach, A. Flores, L. Cucurull and A. Rius, Ionospheric calibration of radar altimeters using GPS tomography, *Geophys. Res. Lett.* **25,** 3771–3774, 1998b.

Ruffini, G., L. P. Kruse, A. Rius, B. Bürki, L. Cucurull, and A. Flores, Estimation of tropospheric zenith delay and gradients over the Madrid area using GPS and WVR data, *Geophys. Res. Lett.* **26,** 447–450, 1999.

Smith, E. K., and S. Weintraub, The constants in the equation for atmospheric refractive index at radio frequencies, *Proc. of the I.R.E.*, 1035–1037, 1953.

Spilker, J., GPS signal structure and performance characteristics, *J. Inst. Navi.*, **25,** 121–146, 1978.

Thayer, G. D., An improved equation for the radio refractive index of air, *Radio Sci.*, **9,** 803–807, 1997.

Ware, R., M. Exner, D. Feng, M. Gorbunov, K. Hardy, B. Herman, Y. Kuo, T. K. Meehan, and W. G. Melbourne, et al., GPS sounding of the atmosphere from low Earth orbit- preliminary results, *Bull. Am. Meteorol. Soc.*, **77,** 19–40, 1996.

Ware, R., C. Alber, C. Rocken, and F. Solheim, Sensing integrated water vapour along GPS ray paths, *Geophys. Res. Lett.*, **24,** 417–420, 1997.

Webb, F. H., and J. F. Zumberge, An introduction to the GIPSY/OASIS II, *JPL Publ.*, **D-11088,** 1997.

Zumberge, J. F., M. B. Heflin, D. C. Jefferson, M. M. Watkins, and F. H. Webb, Precise point positioning for the efficient and robust analysis of GPS data from large networks, *J. Geophys. Res.* **102,** 5005–5017, March 1997.